
# Cold-rolled aluminum foil on nickel mesh as a route to high-performance Raney nickel electrodes for alkaline water electrolysis

International Journal of Hydrogen Energy 218 (2026) 153918

Contents lists available at ScienceDirect

International Journal of Hydrogen Energy

journal homepage: www.elsevier.com/locate/he

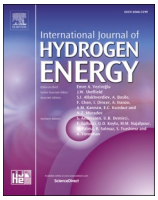

# Cold-rolled aluminum foil on nickel mesh as a route to high-performance Raney nickel electrodes for alkaline water electrolysis

Matthias Gramlich [a,*], Florian Jürries [b,1], Sebastian Hilbert [a], Thomas Rauscher [a], Felix Heubner [a], Christian Bernäcker [a,**], Thomas Weißgärber [a,c]

[a] Fraunhofer Institute for Manufacturing Technology and Advanced Materials IFAM, Dresden Branch, Winterbergstraße 28, 01277, Dresden, Germany
[b] European Synchrotron Radiation Facility, 71, avenue des Martyrs, CS 40220, Cedex 9, 38043, Grenoble, France
[c] TUD Dresden University of Technology, Institute of Materials Science, Helmholtzstraße 7, 01069, Dresden, Germany

ARTICLE INFO

*Keywords:*
Alkaline water electrolysis
Raney nickel
Hydrogen evolution
Electrode development

ABSTRACT

A novel route to produce Raney-nickel-coated electrodes for industrial alkaline water electrolysis is presented, in which aluminum foil is cold-rolled onto a nickel mesh, followed by heat treatment and selective leaching. This process requires no specialized equipment and shows high potential for cost-effective and scalable fabrication of supported Raney nickel electrodes.

Structural analysis with SEM and synchrotron MicroCT confirms the presence of a microporous Raney nickel layer uniformly coating the substrate. Electrochemical characterization reveals superior electrode activity compared to commercial Raney Ni. In 3-electrode setup, overpotentials of 117 mV and 142 mV were recorded at $-0.5$ A/cm$^2$ and $-1$ A/cm$^2$, respectively. Used as cathode in a single cell, a stable cell voltage of 1.65 V at 0.5 A/cm$^2$ after 45 h was measured. A cell voltage of 1.77 V at 1 A/cm$^2$ confirms the excellent activity under industrial conditions.

## 1. Introduction

One of the greatest challenges in the 21st century is transitioning the global economy towards climate neutrality [1]. Because of its ability to be used both as a carbon-neutral energy carrier and a base substance for green steel and chemicals, hydrogen is considered a key component in future value chains. As the demand for green hydrogen is expected to increase significantly in the next decades [2], the question arises of how these large quantities of hydrogen will be produced efficiently. Any viable technology needs to be energy efficient and, considering the expected market ramp-up, highly scalable. As of today, four water electrolysis technologies exist: alkaline electrolysis (AEL), anion exchange membrane electrolysis (AEMEL), proton exchange membrane electrolysis (PEMEL) and solid oxide electrolysis (SOEL). Amongst these technologies, AEL is, as of now, the most economical due to lowest investment cost and longest life time [3,4].

The main catalyst material used for AEL electrodes is nickel (Ni), which is not part of the list of critical materials of the European Union [5]. However, Ni shows only moderate intrinsic catalytic activity towards the hydrogen evolution reaction (HER) [6,7]. One approach to boost the efficiency of Ni electrodes is to improve the kinetics of the HER by making use of the relationship between current density and overvoltage which is described by the Butler-Volmer equation [8]. Accordingly, lowering the current density in turn lowers the overvoltage. An effective reduction of overvoltage can, therefore, be achieved by an increase of the electrochemically active electrode surface area (ECSA). A Ni material with an exceptionally high surface area has been developed by Murray Raney, the so called Raney Ni [9]. Numerous studies have already demonstrated the suitability of Raney Ni as a catalyst for the HER in AEL [10–19] and various processes have been proposed to create Raney-Ni-coated electrodes [11,13,17], [19–27].

Generally, Raney Ni is produced in two subsequent steps: 1) Alloying Ni with either aluminum (Al) or zinc (Zn), and 2) leaching of Al or Zn from the resulting alloy, thereby creating a highly fragmented, defect-rich and microporous structure [9]. To create Raney-Ni-coated electrodes, a substrate must be either coated with a Ni alloy, or a Ni substrate

* Corresponding author.
** Corresponding author.
*E-mail addresses:* matthias.richard.gramlich@ifam-dd.fraunhofer.de (M. Gramlich), christian.bernaecker@ifam-dd.fraunhofer.de (C. Bernäcker).
[1] Permanent address: Chalmers University of Technology, Department of Industrial and Materials Science, 421 96 Göteborg, Sweden.

https://doi.org/10.1016/j.ijhydene.2026.153918
Received 17 November 2025; Received in revised form 4 February 2026; Accepted 5 February 2026
Available online 16 February 2026

is coated with elemental Al followed by heat treatment to form different Ni–Al phases via thermochemical diffusion. All coating methods are followed by a leaching step in a strong alkaline solution.

Ni alloys can be deposited on the substrate with the galvanic route (Ni-Zn) [28–30] or via thermal spraying (Ni–Al). In contrast, elemental Al can be applied to a Ni substrate by means of plasma vapor deposition [21], APS or via powder metallurgy [18]. Thermal spraying of Ni–Al alloys onto suitable substrates by atmospheric plasma spraying (APS) [31] or vacuum plasma spraying (VPS) [22,27] is considered the industrial standard for the production of commercial Raney Ni electrodes (Fig. 1b) [32,33]. However, all these processes require specialized equipment, which makes scale-up challenging.

In this contribution, we explore a new process for producing Raney-Ni-coated electrodes, in which Al foil is applied to a Ni substrate via cold-rolling (roll-to-roll), followed by heat treatment and leaching [34]. As most modern electrolysers in AEL are designed in zero gap configuration and, therefore, require electrodes with advanced geometries, we focus on the application of Ni foil on a woven mesh which meets the zero-gap requirements.

Industry grade furnaces capable of carrying out high-precision heat treatments under controlled conditions are the core component of every powder metallurgic process and are broadly available on the market. Despite the CAPEX of the equipment for cold-rolling and heat treatment, we consider the proposed route easily scalable as all required components are mature and broadly used products. As cold-rolling replaces the APS or PVD step in established routes, high potential for cost reduction in both CAPEX and OPEX is given. Furthermore, the use of Al foil has significant advantages in terms of cost and ease of handling compared to Al powder used in the PVD and the powder metallurgic routes.

The focus of this study is to demonstrate the suitability of the cold-rolling route for producing highly active Raney Ni electrodes with state-of-the-art geometry. Therefore, we analyze the phases formed during heat treatment and subsequent leaching, characterize the resulting microstructure, and investigate the electrocatalytic activity towards HER in both 3-electrode setup and a single cell.

## 2. Material and methods

### 2.1. Material

Commercially available nickel mesh (woven wire cloth) from Haver & Boecker with a wire diameter of 0.25 mm, an aperture width of 0.5 mm and a total thickness of 0.52 mm was selected as the substrate. Three pieces of mesh (10 cm × 4 cm) were coated with Al foil with a thickness of 20 µm, 50 µm or 100 µm. A fourth sample was coated with 50 µm Al foil on both sides. Within this contribution all materials are labeled according to the initial thickness of the applied Al foil.

### 2.2. Process route

The investigated production process consists of three subsequent steps as illustrated in Fig. 1a): Cold-rolling of Al foil onto Ni mesh (1), heat treatment (2) and selective leaching (3).

(1) **Cold-Rolling:** For cold rolling, a calender LaboWalz w200 from Vogt Labormaschinen was used. For each Al foil thickness, the gap between the rollers of the calender was lowered until a permanent connection between mesh and foil via mechanical clamping was established. The connection was strong enough to handle the samples without loosening the foil from the substrate. All samples were introduced with the short side first into the calender. See Table 1 for an overview of the samples produced and the according roller gaps.

(2) **Heat treatment** was carried out at a peak temperature exceeding the Al melting point. The heat treatment protocol was optimized to form predominantly the target phase $Ni_2Al_3$ as this is the only reported phase from which Raney Ni can be formed. Phases with higher Al content ($NiAl_3$) tend to collapse during leaching, while Ni-rich phases (NiAl, $Ni_3Al$) are not affected by strong alkaline solutions [35]. The applied heat treatment protocol was similar to these presented by Bernauer and Konieczny [36,37].

(3) **Leaching:** In order to create the highly fragmented and microporous Raney Ni, Al is removed from the $Ni_2Al_3$ phase using a strong alkali solution according to the following reaction [38]:

$$2Ni_2Al_{3(s)} + 6\,OH^- + 18\,H_2O \rightarrow 4\,Ni_{(s)} + 6\,Al(OH)_4^- + 9\,H_{2(g)} \quad (1)$$

In this contribution, leaching was carried out in a non-stirred solution of potassium hydroxide (25 wt%) and potassium sodium tartrate (10 wt%), with the first 24 h being carried out at room temperature, followed by 6-8 h at 368 K. The purity of the chemicals, as specified by the supplier, was 85 wt% for KOH (acidimetric) and 99 wt% for potassium sodium tartrate (alkalimetric). The concentration of the leaching solution was controlled by titration. Each sample remained in the same solution batch during the entire leaching period. Elevated temperatures are necessary to leach the $Ni_2Al_3$ phase which has been reported to be

**Table 1**
Production parameters of the produced electrode materials.

| Material | Coating/µm Al | Roller Gap/mm |
|---|---|---|
| 20 µm Al | 20 | 0.13 |
| 50 µm Al | 50 | 0.15 |
| 100 µm Al | 100 | 0.2 |
| 2 × 50 µm Al | 2 x 50 | 0.2 |
| Uncoated | - | - |

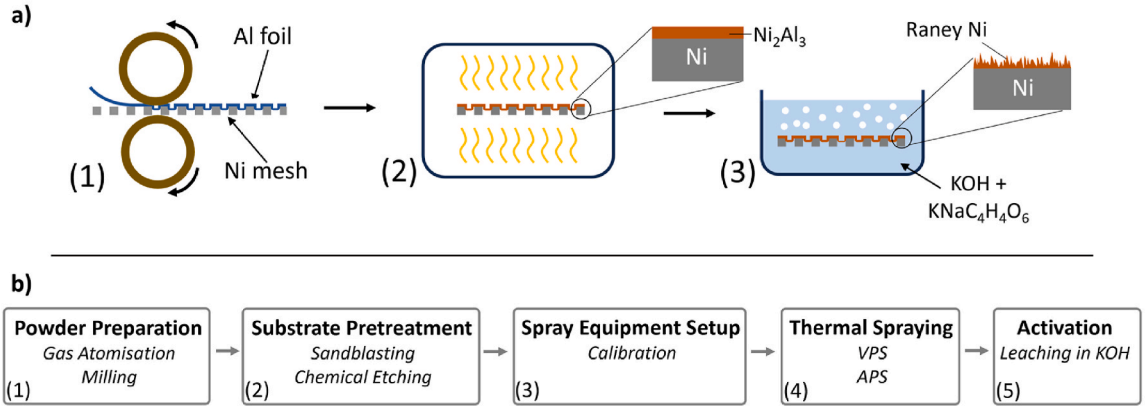


**Fig. 1.** Schematic process routes for Raney Ni electrode production: **a) Cold-rolling route**: (1) cold-rolling, (2) heat treatment, (3) selective leaching **b) Typical thermal spraying route** [22,31,32].

stable against KOH solution at room temperature [35]. For security reasons, leached samples were handled and stored in purified water to avoid exothermic oxidation of adsorbed hydrogen.

Fig. 1b) shows a typical process route for the production of commercial Raney Ni electrodes via thermal spraying and illustrates the higher complexity of this route compared to the presented cold-rolling approach.

### 2.3. ICP-OES

One leaching experiment was carried out under the same conditions as described above with a sample (3.5 × 6 cm) taken from the material produced with 100 μm Al. During the first 6 h, samples of the leaching solution were collected at hourly intervals. After 24 h, another eight samples were taken at 1-h intervals. All samples were subsequently analyzed by inductively coupled plasma optical emission spectroscopy (ICP-OES) to quantify the concentration of dissolved Al in the leaching solution.

### 2.4. Preparation for structural analysis

Before handling samples on air, adsorbed hydrogen remaining on the Raney Ni surface after leaching or the use as electrode for the HER was removed at elevated temperature under vacuum for 24 h. Cross sections for optical and electron scanning microscopy were cut, ground and finally polished.

### 2.5. Optical microscopy

Optical layer thickness determination was used to quantify the thickness of both, the $Ni_2Al_3$ phase after heat treatment and the Raney Ni layer after leaching. Therefore, three cross sections per material were cut. The coating thickness around four Ni wires per cross section was then measured in four directions (left, top, right, bottom), as indicated in Fig. 1, supporting information.

### 2.6. SEM-EDS

Surface and cross sections of the produced materials were characterized by means of scanning electron microscopy (SEM), including energy-dispersive X-ray spectroscopy (EDS), using a Jeol JSM-IT800 SEM equipped with detectors for backscattered (BSD) and secondary electrons (SED) as well as a Bruker XFlash 6/30 SEM-EDS detector for EDS.

### 2.7. X-ray diffraction

The phases formed during heat treatment were characterized by means of X-ray diffraction (XRD) using a Malvern Panalytical Empyrean diffractometer. The diffractograms were recorded using Co radiation (40 kV, 45 mA) in a 2 Theta range of 7 - 140°. The samples (10 × 10 mm) were fixed on a Si single-crystal chip and mounted to the diffractometer with their surface aligned with the diffractometer focusing plane.

### 2.8. Synchrotron MicroCT

In addition to SEM analysis, visualization of the sample volume was achieved by using X-ray Computed Microtomography (CT). This was done at the BM05 beamline of the ESRF using a polychromatic parallel beam with an average energy of 80 keV. For scanning, 4 × 4 $mm^2$ pieces of the electrodes were cut and local tomographic scans were acquired with a pixel size of 0.73 μm on 2048 x 2048 pixel detector, giving a cylindric volume of 1.49 mm in diameter and height. According to the energy and pixel size, the sample-detector distance was set to 100 mm according to the critical propagation distance to maximize phase propagation phase contrast in addition to absorption contrast [39]. The projects were reconstructed by using the Tomwer software [40] using filtered back-projection with single-distance phase retrieval [41]. Visualization of 2D images was performed with ImageJ [42], while 3D volumes were rendered with ParaView (version 5.13.2).

### 2.9. Electrochemical characterization

#### 2.9.1. 3-Electrode setup

Electrochemical characterization was conducted in 3-electrode setup in 30 wt% KOH (aq.) solution at 343 K, mimicking industrial conditions. The KOH solution was prepared from KOH pellets (≥85 wt%, acidimetric), and its concentration was controlled by titration to an accuracy of at least 96% relative to the target concentration. Evolving gases were separated with a two-compartment cell setup consisting of two half cells made of glass which were connected via a separator of Agfa ZIRFON PERL UTP 500. Temperature was controlled by an external thermostat. To remove solved oxygen from the KOH solution, it was purged with nitrogen at least 20 min prior to and during the whole experiment.

For each measurement, one sample (3.4 × 1 cm) of the leached material was attached to a custom-built sample holder [18] exposing 2 $cm^2$ of geometric area of the electrode to the electrolyte. Coiled platinum wire was used as the counter electrode, while a Reversible Hydrogen Electrode (RHE) served as reference electrode due to its ability to provide the reversible hydrogen potential according to pH and temperature of the electrolyte it is placed in. The RHE was installed inside a Haber-Luggin-capillary in the same solution as the working electrode so that the distance between tip of the capillary and working electrode was approximately 5 mm to minimize the uncompensated ohmic resistance $R_u$. A Gamry Reference 3000 potentiostat was used and all experiments were IR-drop corrected using the current interrupt method. The current densities applied and measured within all experiments refer to the geometric sample area of 2 $cm^2$ if not otherwise indicated.

To study the HER activity, all materials were benchmarked with a custom protocol consisting of galvanostatic measurements (GS) to determine the overpotential $\eta$ at a given current density, Tafel analysis to describe the potential-current density behavior and cyclic voltammetry (CV) to examine the double-layer capacitance $C_{dl}$:

1. **GS**: −500 mA/$cm^2$ for 5 h
2. **Tafel analysis:** $-500 < j_{max} < -1$ mA/$cm^2$
3. **GS**: −1000 mA/$cm^2$ for 5 h
4. **Tafel analysis:** $-1000 < j_{max} < -1$ mA/$cm^2$
5. **CV preconditioning 1:** 4 cycles $0 < E_{RHE} < 1$ V, scan rate of 1 mV/s
6. **CV preconditioning 2**: Potentiostatic at 0.4 V for 20 min
7. **CV**: $350 < E_{RHE} < 450$ mV, scan rates between 0.01 and 0.07 V/s

The current applied to the working electrode during the galvanostatic and Tafel steps led to the evolution of hydrogen gas on the working electrode according to reaction equation of the HER in alkaline media:

$$2H_2O + 2e^- \rightarrow 2OH^- + H_2 \quad (2)$$

As the potential $E_{RHE}$ was measured against an RHE, it is equivalent to the negative overpotential of the HER at the given environmental conditions as $E_{rev,RHE} = 0\ V$:

$$E_{RHE} = E_{rev,HER} - \eta = -\eta \quad (3)$$

To evaluate the potential-current density behavior by means of Tafel analysis, $E_{RHE}$ was measured at various current densities for 20 s each (step 2 and 4). The current density was first set to the maximum of the given step (either −500 or −1000 mA/$cm^2$) and subsequently lowered to the minimum of −1 mA/$cm^2$. The mean of $E_{RHE}$ over the last 10 s of each measurement was plotted against the corresponding current density on a semi-logarithmic scale, resulting in the well-known Tafel plot.

The reaction kinetics of the HER were further investigated by

applying linear fits to the linear regions of the Tafel plot as the slope of these fits can reveal the rate determining step (RDS) of the observed reaction. Within the HER mechanism in alkaline media, three possible RDS exist [10]:

$$\text{Volmer step}: M + H_2O + e^- \rightarrow MH + OH^- \quad (4)$$

$$\text{Heyrowsky step}: MH + H_2O + e^- \rightarrow M + H_2 + OH^- \quad (5)$$

$$\text{Tafel step}: MH + MH \rightarrow 2M + H_2 \quad (6)$$

The theoretical Tafel slopes for a reaction limited by the Volmer, Heyrowsky or Tafel step at 343 K (assuming a transfer coefficient $\alpha = 0.5$) were calculated to be 136, 45 and 34 mV [8] and were compared to the slopes obtained from fits to the experimental data.

Cyclovoltammetry was used to determine the electrochemically active surface area (ECSA) [43,44]. Prior to applying this method, the sample was preconditioned, first by cyclic voltammetry to remove ad- and absorbed hydrogen species (step 5) and subsequently by bringing it into an equilibrium state at 0.4 $V_{RHE}$ (step 6). According to McCrory no faradaic processes are expected to occur at this potential on Ni [44]. After the two preconditioning steps, the potential was cyclically changed with ±50 mV at varying scan rates $\nu$ around 0.4 $V_{RHE}$. The mean current density at 0.4 V at each scan rate was calculated as:

$$j_{mean} = \frac{(|j_{anodic}| + j_{cathodic})}{2} \quad (7)$$

The slope of a line through the data points in a $j$-$\nu$-plot equals the double layer capacitance $C_{dl}$ according to Trasatti [43] (Q – charge):

$$i = \frac{dQ}{dE}*\frac{dE}{dt} = C_{dl}*\nu \quad (8)$$

With the double-layer capacitance of uncoated Ni mesh ($C_s$) the roughness factor $R_f$ was then calculated describing the enlargement of the surface area caused by the Raney Ni coating.

$$R_f = \frac{C_{dl}}{C_s} \quad (9)$$

The material selected for the single cell experiment was also evaluated by electrochemical impedance spectroscopy (EIS) in a separate measurement to further investigate its kinetic behavior towards the HER. Galvanostatic EIS measurements were performed at current densities of −300, −400 and −500 mA/cm$^2$ over frequencies from 5 kHz to 0.05 Hz. Prior to each EIS measurement, the electrode was conditioned at the corresponding current density for 5 min to establish stable conditions (Fig. 11, supporting information). The obtained impedance data was analyzed in the Nyquist representation (−Z" vs. Z') and fitted with an equivalent circuit containing a constant phase element (CPE) to extract the uncompensated ohmic resistance $R_s$, the polarization resistance $R_p$ and/or the charge transfer resistance $R_{ct}$ using the Gamry Echem Analyst software (version 7.8.4).

#### 2.9.2. Single cell

Two experiments were conducted to evaluate the behavior of a Raney Ni electrode produced via the presented process route in a single micro-flow cell (MFC). Except for the electrode material on the cathode side, the experiments were set up identically: One with a Raney-Ni-coated electrode from the material produced with 100 µm Al foil and one with uncoated Ni mesh as cathode.

The MFC was assembled in zero gap design in which the geometric electrode area amounted to 10 cm$^2$. Ni foam with an average pore size of 580 µm was used as porous transport layer (PTL) between current collectors and electrodes while ZIRFON PERL 500+ was installed as diaphragm. Ni felt coated with a layer of NiFe-LDH as described by Li [45] was used as the anode. The electrolyte consisted of 30 wt% KOH solution with the concentration controlled as described in chapter 2.8.1 at 343 K and was circulated with an upstream flowrate of 76 ml min$^{-1}$ cm$^{-2}$. The electrolyte temperature was controlled with a heating hose.

Except for the current collectors consisting of solid Ni plates, no metallic components were in contact with the electrolyte to avoid any contamination with iron or chromium impurities that might leach out from metallic components [46].

The high frequency resistance $R_{hf}$ that represents the ohmic cell resistance was measured with electrochemical impedance spectroscopy (EIS) at open circuit potential (OCP), both at the beginning (BoT) and the end (EoT) of the experiment. $R_{hf}$ was measured to be 17 mΩ in the setup with the Raney Ni electrode, and 22 mΩ in the experiment with the uncoated Ni mesh (BoT) and 12.5 mΩ and 16 mΩ (EoT), respectively. The electrochemical protocol consisted of four steps:

1. **Galvanostatic pretreatment:** 100 mA/cm$^2$ for 30 min
2. **Polarization curve:** with $0.2 < j < 1000$ mA/cm$^2$
3. **Galvanostatic stability:** 500 mA/cm$^2$ for 45 h
4. **Polarization curve:** $0.2 < j < 1000$ mA/cm$^2$

Purified water was added to the electrolyte during step 3 with a rate of 1.679 ml/h to balance the water consumed by electrolysis.

## 3. Results and discussion

### 3.1. Microstructure after heat treatment

During heat treatment of the cold-rolled samples, a thermochemical reaction between Ni and Al is initiated, which leads to the formation of different Ni–Al phases. As the stoichiometry and morphology of these phases significantly influence the properties of the Raney Ni layer generated by their leaching, a detailed characterization of these phases is essential for understanding the microstructure-property relationship of the electrodes.

Fig. 2 shows cross sections through a single wire of the mesh from samples of all produced materials after heat treatment. The bright Ni core is surrounded by a layer of one or more Ni–Al phases. After determining the Ni and Al content of each phase by means of multiple SEM-EDS point scans per phase, they were identified based on the Ni–Al phase diagram [47–49]. While the number of observed phases differs within the set of investigated materials, the sequence of phases from the core to the surface remains consistent across all materials: An innermost layer of $Ni_2Al_3$, followed by $NiAl_3$ and, finally, an Al layer with $NiAl_3$ precipitates.

In the sample produced with 20 µm Al foil (Fig. 2, a), only $Ni_2Al_3$ is observed on top of the Ni core while the sample with 50 µm Al foil contains another thin layer of $NiAl_3$ on top of $Ni_2Al_3$ (Fig. 2, b). For the samples with 2 × 50 or 100 µm Al, all three layers ($Ni_2Al_3$, $NiAl_3$, Al + $NiAl_3$) are present (Fig. 2c and d).

In these micrographs, $Ni_2Al_3$ is the dominant phase by area, consistent with previous studies reporting it to be the fastest-growing phase in the Ni–Al system [21,50,51]. Since formation and growth of Ni–Al phases are diffusion controlled [50–52], the extend of $Ni_2Al_3$ formation is limited by the temperature-time protocol of the heat treatment step. The temperature must be sufficiently high to permit solid-state diffusion, thereby enabling the evolution of the Ni–Al phases. According to Alimadadi et al. who studied the evolution of Ni–Al phases during thermochemical diffusion in detail [50], the $Ni_2Al_3$ phase grows between the interface of Ni and Al until all available Al is transformed. Under the given conditions this was the case only for the material with 20 µm Al. In the other materials, a layer of Al and $NiAl_3$ precipitates remains on top of the $Ni_2Al_3$ phase, because within the applied heat treatment, the reaction was stopped before all Al could be transformed.

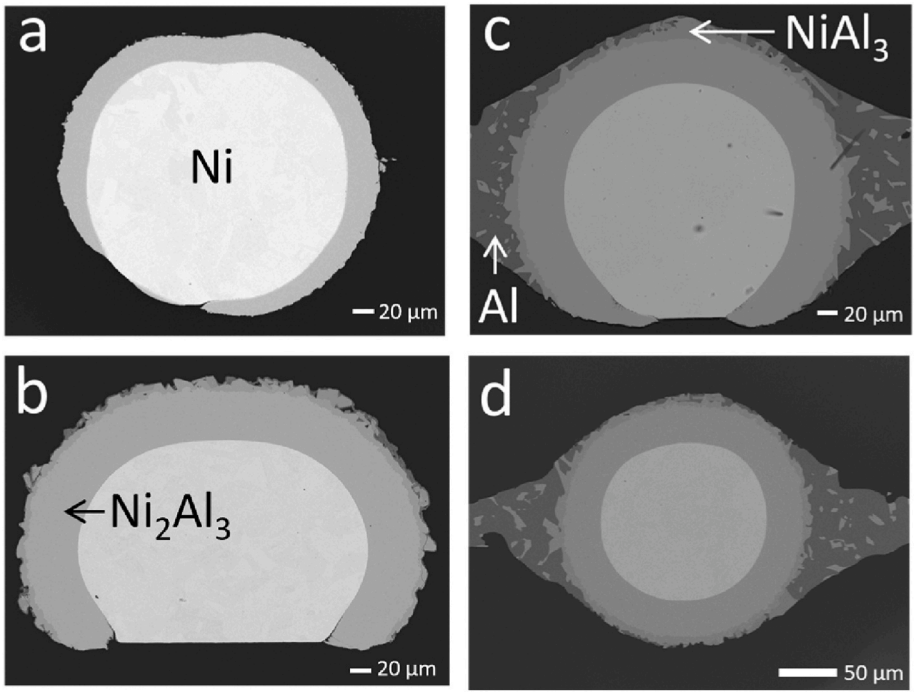


**Fig. 2.** SEM micrographs taken with a BSE detector of cross sections of samples after heat treatment. Phase analysis with SEM-EDS. a) 20 µm Al, b) 50 µm Al, c) 100 µm Al, d) 2 × 50 µm Al.

These observations are further strengthened by XRD measurements (Figs. 2–9, supporting information). The $Ni_2Al_3$ phase was detected in all materials, $NiAl_3$ in all but the material produced with 20 µm Al foil and Al only in the materials with 100 or 2 × 50 µm Al, which is in line with the findings from SEM-EDS. See the supporting information for the diffractograms with labeled peaks and corresponding pattern views resulting from phase analysis.

$Ni_2Al_3$ has been reported to be the most stable phase after selective leaching in alkaline solutions and is, therefore, the target phase to form the Raney Ni [35]. Accordingly, it is of great interest to understand the thickness and distribution of this phase in the heat-treated materials. The results of optical layer thickness analysis of the $Ni_2Al_3$ phase are plotted in Fig. 3a). The values of its thickness vary strongly within the sample with 20 µm Al foil, with a maximum of approximately 30 µm, while samples with higher Al content show a more uniform coating of approximately 46 µm on left, right and top. The bottom remains uncovered in the sample with 50 µm Al, partially covered in the sample with 100 µm Al, and completely covered in the sample with 2 × 50 µm Al.

The nearly identical thickness of $Ni_2Al_3$ in the materials produced with 50, 100 or 2 × 50 µm Al foil is due to the diffusion-controlled evolution of this phase. As the same heat treatment protocol was applied to all materials, the maximum thickness of $Ni_2Al_3$ was limited by time and temperature. Provided that Al is not fully consumed, it can be concluded that the average thickness $Ni_2Al_3$ is independent of the remaining amount of available Al and only determined by the heat treatment protocol.

Accordingly, the thickness of the resulting Raney Ni layer is controlled by two factors: 1) the thickness of the applied Al foil and 2) the heat treatment protocol. While the thickness of the Al foil was the limiting factor only for the material produced with 20 µm Al foil, the heat treatment protocol controlled the Raney Ni layer thickness in all other produced materials as it interrupted the formation of the $Ni_2Al_3$ phase before all available Al could be transformed. See Fig. 4 for a schematic representation of the phase evolution and transformation process during heat treatment with Al foils of different thicknesses.

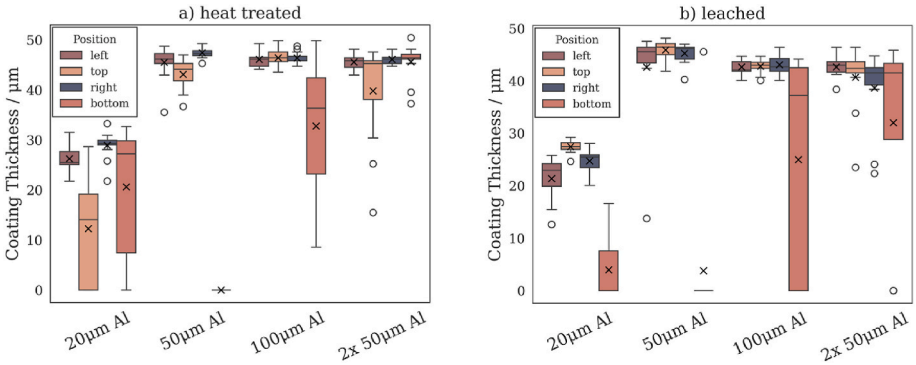


**Fig. 3.** Boxplots with thickness of the coating layer on the Ni substrate measured with optical microscopy. 12 data points per box. Boundaries of the boxes indicate the 25th and 75th percentile, central lines the median and **X** the mean. Outliers are shown as **O**. a) $Ni_2Al_3$ phase (heat-treated), b) Raney Ni layer (leached).

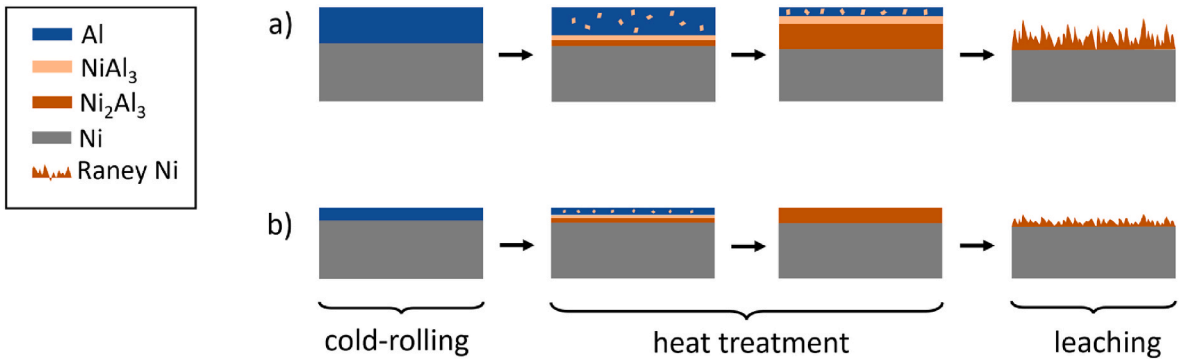


**Fig. 4.** Schematic processes of the evolution of microstructure and phases formed during heat treatment and leaching. a) 50 or 100 or 2 × 50 μm Al foil, b) 20 μm Al foil.

Fig. 4a) shows the process observed for the materials produced with 50, 100 and 2 × 50 μm Al foil and Fig. 4b) represents the process of the material coated with 20 μm Al.

### 3.2. Microstructure after leaching

The thickness and distribution of the Raney Ni layer formed by selective leaching is plotted in Fig. 3b) and reflects the results from the heat-treated samples. Notably, the former $Ni_2Al_3$ phase has been transformed into a skeletal Raney Ni phase of a similar thickness. This observation indicates that $NiAl_3$ and Al are dissolved during leaching, which aligns with findings in the literature [35,38,53]. Accordingly, the $Ni_2Al_3$ phase is the main precursor of the Raney Ni layer so the focus of heat treatment must lie in optimizing thickness and distribution of the $Ni_2Al_3$ phase as it will significantly determine the final structure of the Raney-Ni-coated electrodes.

Micrographs from the surface of the electrode produced with 50 μm Al foil are displayed in Fig. 5. It reveals three distinct regions of interest: 1) long, straight and deep microcracks with widths of up to 10 μm; 2) a broad irregular network of narrower cracks; and 3) fine-grained regions characterized by a micro-to nanocrystalline morphology, forming a highly irregular and rough surface texture. These observations are comparable to similar characteristics of Raney type structures reported in the literature [13,18,19,25,54]. SEM-EDS analysis of cross sections of leached materials revealed a remaining Al content of approximately 10 at% in the coating layer which lies far below the 60 at% Al in the initial $Ni_2Al_3$ phase. It is concluded that the leaching step has effectively removed a significant share of Al from $Ni_2Al_3$ resulting in the described Raney Ni structure. The remaining Al is located within the bulk material at greater distance from the surface and, therefore, cannot be removed by chemical leaching.

MicroCT scans of the leached materials were acquired to gain insight into the overall structure of the Raney Ni layer on the substrate. For each material, Fig. 6 shows both the 3D volume and a cross section through this volume in x-z plane. Clearly, the Raney-type structure is present on all samples and is connected to the Ni mesh which creates the electrical contact needed for the application as electrode. In the cross sections, a mostly uniform Raney Ni layer is visible in the samples produced with 50, 100 or 2 × 50 μm Al foil which covers the whole substrate. Notably, the Raney Ni layer is present all over the Ni wires, even though initially plain Al foil was cold-rolled on a non-flat substrate. These scans confirm that connecting Ni mesh and plain Al foil only by uniaxial mechanical pressure, followed by heat treatment and leaching, results in a uniform Raney Ni layer that envelopes the wires of the Ni substrate.

The concentration of Al in the leaching solution for one sample of the 100 μm Al material is shown in Fig. 10, supporting information. As Al in the leaching solution can only originate from dissolution of the heat-treated material, the measured concentration directly reflects the leaching process. During leaching at 298 K, a sharp increase in the Al concentration is observed during the first 4 h, followed by a moderate increase over the next 20 h. After the temperature was raised to 368 K, the Al concentration increased at a higher rate over several hours. From these observations, two conclusions can be drawn: 1) Substantial amounts of Al are leached out from the heat-treated material, and 2) elevated temperatures induce an additional leaching step which most likely would not occur at 298 K, as reported in the literature [35].

### 3.3. Electrochemical properties

#### 3.3.1. Electrocatalytic activity towards HER

The galvanostatic performance in 3-electrode setup at −0.5 and −1 A/cm$^2$ is displayed in Fig. 7. All Raney-Ni-coated electrodes show

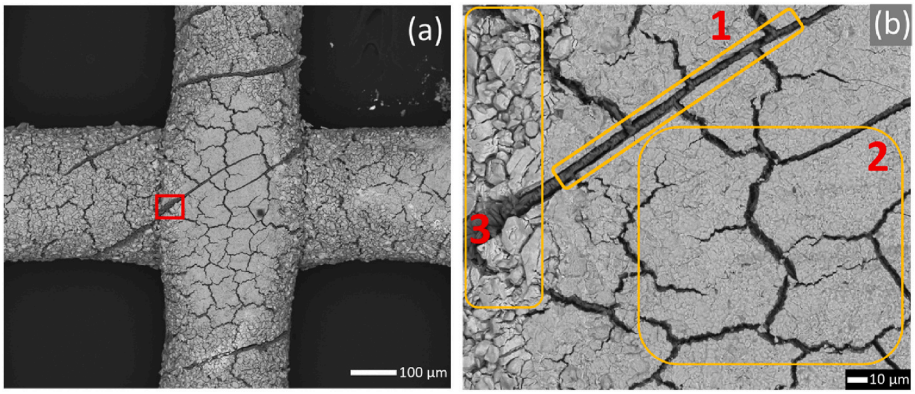


**Fig. 5.** SEM micrograph of the surface of material produced with 50 μm Al foil after leaching. Acquired with backscattered electron detector at 15 kV. (a) overview, (b) zoomed view of the red box in (a)

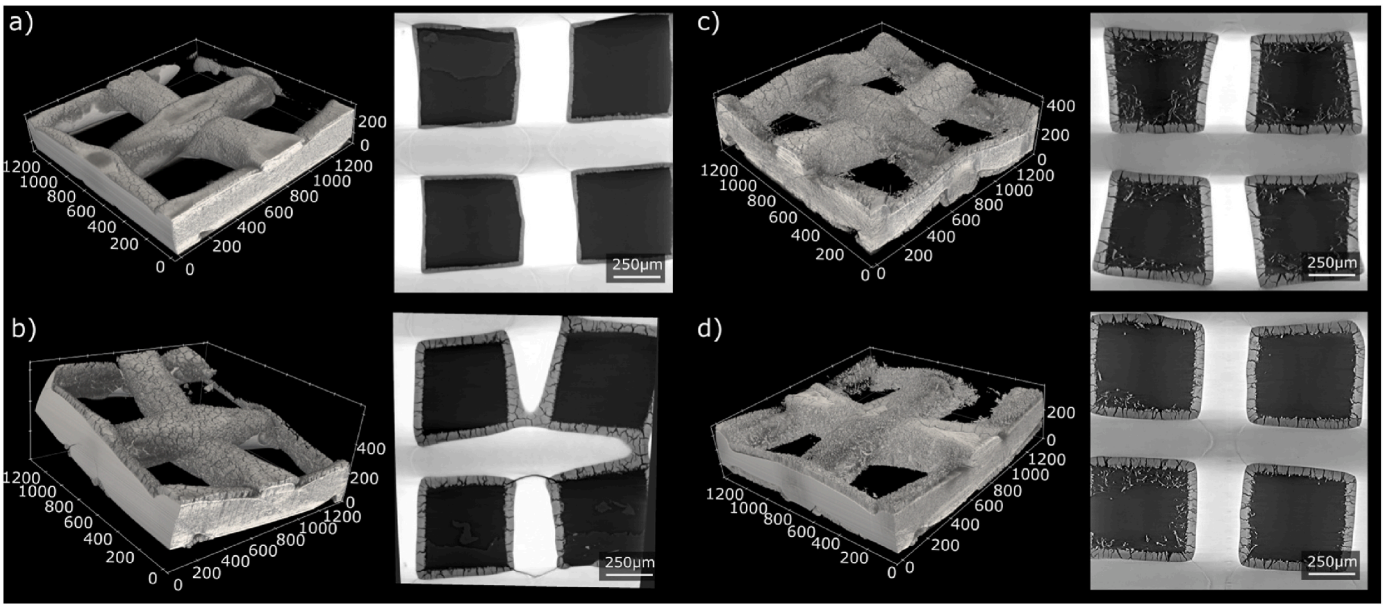


**Fig. 6.** MicroCT images. Reconstructed 3D volumes (left) and cross section through x-y-plane (right) a) 20 µm Al, b) 50 µm Al, c) 100 µm Al, d) 2 × 50 µm Al.

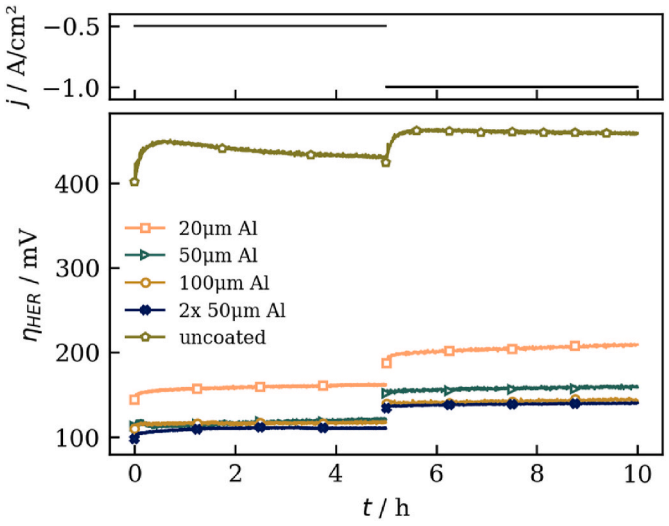


**Fig. 7.** Overpotential-time curves (η - t) of galvanostatic measurements at −0.5 and −1 A/cm$^2$ for 5 h each. 30 wt% KOH solution at 343 K, $N_2$ purged.

significantly lower overvoltages towards the HER than the uncoated Ni mesh, outperforming it by a factor of up to 3.7 at −0.5 A/cm$^2$. The lowest overvoltages are recorded for the samples produced with 2 × 50 µm and 100 µm Al foil, which show a similar activity. Notably, the electrodes with the lowest overvoltage also tend to be the most stable ones, showing the least potential drift over time. The decrease in overpotential of the bare Ni mesh over time can be attributed to both the reduction of Ni oxide species [55] and the deposition of iron from the electrolyte on the electrodes surface, thereby increasing the active area [46,56,57]. See Table 3 for a summary of the electrochemical properties, including the overpotentials after 5 h at each current density.

Overvoltages reported for Raney Ni electrodes in the literature are typically measured under different experimental conditions, such as setup, temperature, and electrolyte concentration, due to the lack of standardization in 3-electrode measurements. Since these parameters directly influence the measured potential, comparisons between reported overvoltages must be drawn with caution and can only serve as indicators. Table 2 summarizes overvoltages reported for various Raney Ni electrodes, including substrate materials, fabrication methods, and test conditions. The electrodes developed in this work show overvoltages that are either comparable to or significantly lower than those reported for Raney Ni electrodes in the literature, indicating similar or enhanced electrocatalytic activity towards the HER. Based on these results, it is concluded that the presented electrodes are comparable with established materials, either by providing higher activity or by achieving similar activity with a substantially simpler and more cost effective production process.

**Table 2**
Overvoltages toward the HER of different Raney-Ni-coated electrodes in the literature and the corresponding experimental conditions. The last row includes data from the present work.

| Substrate | Process | $T$/K | $c_{KOH}$/ wt.% | $j$/mA/ cm$^2$ | $\eta_{HER}$/ mV | |
|---|---|---|---|---|---|---|
| Ni plate | PVD | 298 | 5.4 | −100 | 123 | [21] |
| Perforated Ni sheet | VPS | 343 | 25 | −1000 | 120-140 | [22] |
| Ni expanded mesh | Powder metallurgy | 333 | 30 | −300 | 118 | [18] |
| Ni plate | Hot dip galvanizing | RT | 30 | −100 | 130 | [58] |
| Ni foil | Cold-Rolling | RT | 32 | −100 | 192 | [23] |
| **Ni mesh** | **Cold-Rolling (100 µm Al)** | **343** | **30** | **−500** | **117** | |

**Table 3**
Calculated values of $C_{dl}$ and $R_f$ obtained from CV data, overpotential $\eta_{500}$ and $\eta_{1000}$ measured after 5h each at −500 and −1000 mA/cm$^2$, and absolute Tafel slopes in the current density regions −30 to −100 mA/cm$^2$ and –150 to −500 mA/cm$^2$ 30 wt% KOH solution at 343 K, $N_2$ purged.

| Sample | $C_{dl}$/ mFcm$^{-2}$ | $R_f$/- | $\eta_{500}$/ mV | $\eta_{1000}$/ mV | $\lvert b_{30\text{-}100}\rvert$/ mV dec$^{-1}$ | $\lvert b_{150\text{-}500}\rvert$/ mV dec$^{-1}$ |
|---|---|---|---|---|---|---|
| uncoated | 7.6 | 1 | 404 | 431 | 137 | 130 |
| 20 µm Al | 101.5 | 13 | 162 | 209 | 88 | 69 |
| 50 µm Al | 241.3 | 32 | 120 | 158 | 40 | 92 |
| 100 µm Al | 290.9 | 38 | 117 | 142 | 38 | 78 |
| 2 × 50 µm Al | 302.4 | 40 | 110 | 140 | 37 | 76 |

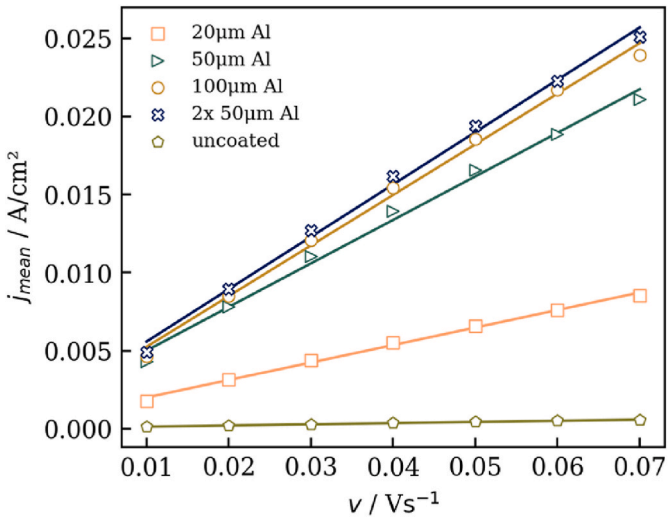


**Fig. 8.** Mean ($j_{mean}$) of the absolute values of anodic and cathodic current density at 0.4$V_{RHE}$ versus scan rate (v). 30 wt% KOH solution at 343 K, $N_2$ purged.

### 3.3.2. Determination of the active surface area

The double layer capacitance $C_{dl}$ serves as a measure for the electrochemical active surface area (ECSA). $C_{dl}$ was acquired from the slope of a linear fit through data points of the mean current density at 0.4 V measured during cyclic voltammetry over the according scan rates (Fig. 8). The slope is highest for the electrodes manufactured with 100 µm and 2 × 50 µm Al foil, followed in descending order by the electrodes with 50 and 20 µm Al and finally the uncoated mesh. From these $C_{dl}$ values, the roughness factor $R_f$ was calculated (Table 3) to compare the active surface area of the Raney-Ni-coated electrodes with that of uncoated Ni mesh. Highest $R_f$ values were obtained for the electrodes manufactured with 2 × 50 µm and 100 µm Al foil with 40 and 38, respectively. These values demonstrate the significant increase of the ECSA achieved by coating the substrate with a Raney Ni layer.

### 3.3.3. Tafel analysis and HER kinetics

Tafel plots of all Raney Ni electrodes and the uncoated Ni mesh are provided in Fig. 9 with both the geometric current density and the real current density ($j_{real} = j_{geo}/R_f$) based on the determined ECSA via CV (normalized Tafel plot). In the plot with geometric current densities (Fig. 9, left), electrodes produced with 50, 100 and 2 × 50 µm Al foil result in very similar curves, while the electrode with 20 µm Al and the uncoated mesh show a consistently higher potential across all current densities.

Interestingly, in the normalized form of the Tafel plot (Fig. 9, right), all curves lie practically on top of each other. This observation demonstrates that the electrocatalytic activity of the Raney Ni electrodes is a purely extrinsic effect, driven by enlargement of the active surface area available for HER. No evidence of intrinsic, material-dependent effects distinguishing the catalytic behavior of uncoated Ni mesh and Raney Ni electrodes was found.

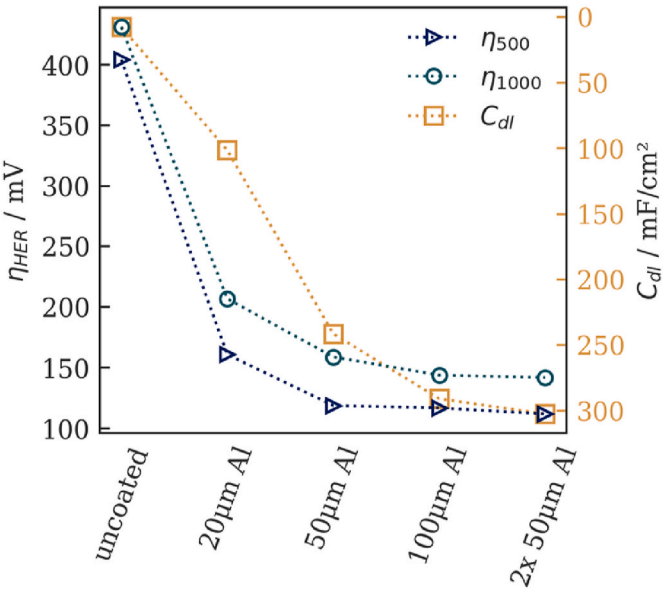


**Fig. 10.** Comparison of overvoltages ($\eta_{500}$ and $\eta_{1000}$) after 5 h each at −500 and −1000 mA/cm² and the double layer capacitance ($C_{dl}$).

In the Tafel plots in Fig. 9 (left) two linear regions could be determined for the Raney-Ni-coated materials (−30 to −100 mA/cm² and –150 to −500 mA/cm²). The resulting apparent Tafel slopes are summarized in Table 3 as absolute values. The Tafel slopes of the uncoated Ni mesh are very close to the theoretical slope of the Volmer step at 343 K (136 mV $dec^{-1}$), indicating that the electrochemical adsorption of hydrogen is the rate determining step (RDS).

In contrast, the Raney-Ni-coated electrodes produced with 50, 100 and 2 × 50 µm Al show significantly smaller Tafel slopes at low current densities, indicating Tafel or Heyrowsky dominated kinetics. At higher currents the slopes range between the theoretical values of the Heyrowsky and the Volmer step, indicating mixed contributions of the RDS, a growing influence of gas bubble coverage or local mass transport. The electrode produced with 20 µm Al foil exhibits intermediate Tafel slopes at all current densities, indicating a less ideal kinetic behavior towards the HER. Generally, the Tafel analysis supports the observation that HER kinetics are strongly improved by the Raney Ni coating.

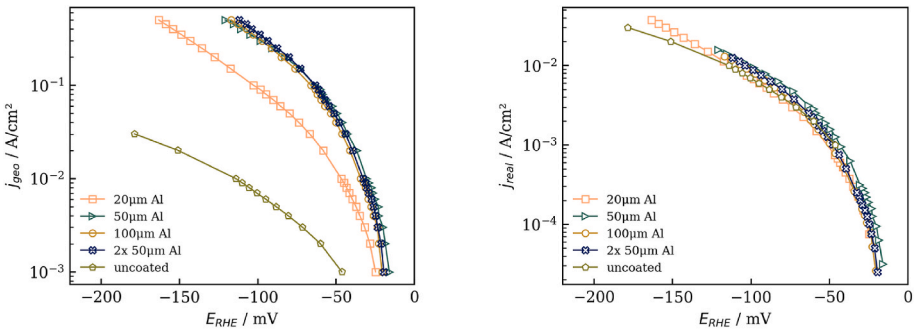


**Fig. 9.** Tafel plots with semilogarithmic j-E curves, with $-0.5 < j_{geo} < -0.001$ A/cm². Left: Geometric current density. Right: Normalized Tafel plot using the real current density $j_{real}$ based on the roughness factor.

The material produced with 100 µm Al was further analyzed by galvanostatic EIS at −300, −400 and −500 mA/cm$^2$ (Fig. 12, supporting information). The resulting Nyquist plots show a single depressed semicircle per EIS spectrum, and the polarization resistances were calculated to be 57, 47 and 40 mΩ, respectively. These findings indicate the fast electrode kinetics, while the absence of additional low frequency features suggests that charge-transfer processes dominate the impedance response under the given conditions ($R_p \approx R_{ct}$). This is consistent with the low observed Tafel slopes for this electrode.

### 3.4. Microstructure-property relationships

Overvoltages and double layer capacitances summarized in Table 3 are visualized in Fig. 10. The plot reveals a correlation between the amount of applied Al and both $C_{dl}$ and $\eta$. This relationship aligns with the observed Raney Ni distribution shown in Figs. 3 and 6, as the active area and, hence, $C_{dl}$ is expected to increase with both the thickness and degree of coverage of the Raney Ni layer. Optical layer thickness analysis and MicroCT scans indicate that electrodes produced with 20 µm Al exhibit the lowest Raney Ni layer thickness and degree of coverage. Materials produced with 50, 100 and 2 × 50 µm Al foil show similar Raney Ni layer thicknesses, but with increasing degree of coverage. These observations explain the correlation in Fig. 10: As the amount of applied Al increases, $C_{dl}$ increases and $\eta$ decreases, reflecting improved electrode performance due to enhanced active surface area.

This correlation further supports the finding from the normalized Tafel plot that the activity of the Raney Ni electrodes is determined by extrinsic effects. We conclude that the microstructure of the Raney Ni electrodes presented in this contribution is the key factor explaining the exceptionally enhanced catalytic activity towards the HER.

As the geometry and spatial distribution of the Raney Ni layer is determined by both, the Al foil dosage and the applied heat treatment protocol, both need to be considered simultaneously when further optimizing the process route. While the Al foil defines the potentially achievable limits of the Raney Ni thickness and distribution, heat treatment controls the actual formation of the $Ni_2Al_3$ phase and thus the final Raney Ni layer.

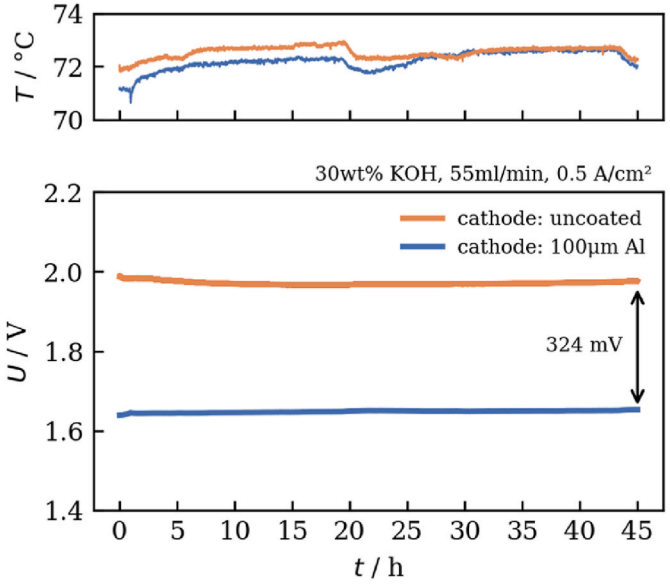


**Fig. 11.** Cell voltage and temperature of MFC measurements using Raney Ni or uncoated Ni mesh as cathode at 0.5 A/cm$^2$ for 45 h. 30 wt% KOH, 55 ml/min.

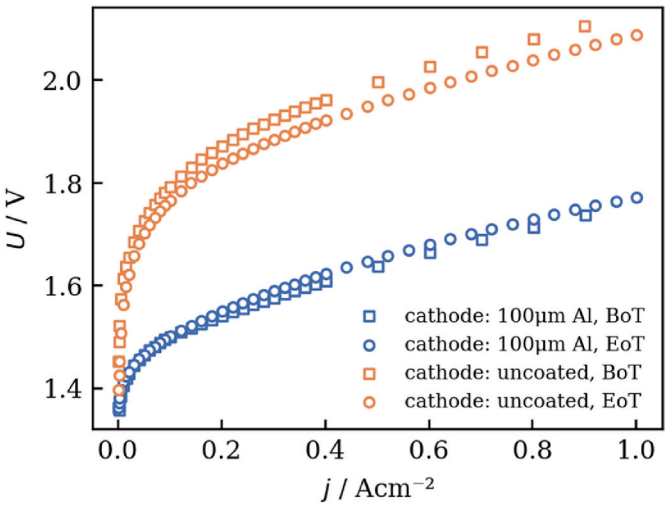


**Fig. 12.** Polarization curves before and after the stability test recorded in a MFC with Raney Ni or uncoated Ni mesh as cathode. 30 wt% KOH, 55 ml/min.

### 3.5. Performance in a single cell

The electrode produced with 100 µm Al foil was selected for performance testing in a single micro-flow cell (MFC), as it offered the best combination of catalytic activity and processability during cold-rolling, requiring only a single foil compared to the two used in the 2 × 50 µm configuration. The results of a galvanostatic stability test at 0.5 A/cm$^2$ for 45 h and the polarization curves before (BoT) and after the stability test (EoT) are plotted in Figs. 11 and 12. With a cell voltage of 1.65 V after 45 h, the setup with the Raney Ni electrode outperforms the uncoated Ni mesh by 324 mV after the same time (Fig. 11). As no other parameter except the cathode material were changed and because the temperature was kept nearly identical in the two measurements, it is concluded that the improved performance is only due to the activity of the cathodes.

The values measured for $R_{hf}$ drop slightly over the period of both experiments (chapter 2.9.2). This observation is attributed to the more evenly heated cell at the end of the test and the local formation of highly conductive nickel oxides on the anode side at the contact points between PTL and backplate which both result in a decrease of ohmic resistance. The values of $R_{hf}$ are generally small (12.5 to 22 mΩ) and so is its impact on the cell voltage. Therefore, it is concluded that the cell setup remained stable during both experiments and the changes in cell voltage can be attributed to the properties of the installed electrodes.

In both MFC measurements the cell voltage remained almost constant. The voltage of the setup with the uncoated Ni cathode dropped slightly during the first hours, which can either be caused by the

**Table 4**
Comparison of the measured cell voltage with similar systems reported in the literature including electrode materials, electrolyte concentration, temperature, current density and cell voltage.

| Cathode | Anode | $c_{KOH}$/ wt.% | T/K | j/A/ cm$^2$ | $U_{cell}$/ V | |
|---|---|---|---|---|---|---|
| Commercial Raney Ni mesh | Commercial Raney Ni mesh | 30 | 253 | 0.5 | 1.8 | [32] |
| Raney Ni (VPS) on Ni foam | NiFe-LDH on Ni foam | 30 | 253 | 0.5 | 1.75 | [59] |
| Raney Ni (APS) | Raney Ni–Mo (APS) | 30 | 243 | 0.5 | 1.8 | [31] |
| Raney Ni–Mo (VPS) | Raney Ni (VPS) | 24 | 253 | 0.5 | 1.75 | [22, 33] |
| **Cold-rolled Raney Ni mesh** | **NiFe-LDH on Ni felt** | **30** | **245** | **0.5** | **1.65** | |

conditioning processes discussed in chapter 3.3.1 or by an increase of temperature which can result in higher electrolyte conductivity and electrode activity. As voltage and temperature correlate strongly in this experiment, we attribute this observation mainly to the temperature effect.

In the setup with the Raney-Ni-coated electrodes, the cell voltage increased by 8 mV over 43.5 h, excluding the conditioning step in the first 1.5 h. The stability of the investigated Raney-Ni-coated electrode is considered a promising starting point for further improvement.

The superior activity of the Raney-Ni-coated electrodes is also demonstrated by the polarization curves in Fig. 12 as they lie significantly lower than the curves recorded with the uncoated Ni electrode. With a voltage of 1.77 V at 1 A/cm$^2$ (EoT), the Raney Ni electrode exhibits excellent performance even at elevated current densities.

As the voltage difference between the setups with uncoated and Raney-Ni-coated cathode in the MFC is very similar to the results in 3-electrode setup (Table 3), the latter is confirmed to be a suitable method for approximating the electrode behavior in the MFC.

Table 4 compares the cell voltage of the presented material system with that of similar materials reported in the literature. Especially a comparison with state-of-the-art commercial Raney Ni electrodes is of interest. As electrode manufacturers only provide limited publicly available data on electrode activity, literature reports on Raney Ni electrodes produced by thermal spraying were selected. Thermal spraying (APS or VPS) represents the standard manufacturing route for commercial Raney Ni electrodes and is therefore considered a suitable benchmark.

Notably, the cell measurement presented in this contribution shows the lowest cell voltage within this comparison, despite being conducted at a lower temperature (245 K) than most of the reported measurements (253 K). Considering the influence of temperature on the cell voltage, it can be concluded that the presented material system clearly outperforms commercial Raney Ni electrodes. Accordingly, the presented approach provides a simpler process route compared to the industrial standard while simultaneously resulting in notably more active Raney Ni electrodes.

## 4. Conclusion

In this contribution, Raney-Ni-coated electrodes for use as cathodes in alkaline water electrolysis were successfully fabricated via a novel cold-rolling route, in which Al foil is applied to a Ni mesh, followed by heat treatment and leaching. Electrochemical and microstructural characterizations of the produced materials led to the following key findings:

- Cold-rolling Al foil onto Ni mesh establishes a mechanically stable connection between Ni and Al.
- During heat treatment, Ni–Al phases form, with $Ni_2Al_3$ identified as predominant phase.
- Selective leaching of the heat-treated materials leads to a micro-to nanostructured Raney Ni layer, which envelops the wires of the Ni mesh.
- MicroCT analysis confirms the uniform distribution of the Raney Ni layer with consistent thickness across the entire substrate.
- These Raney-Ni-coated electrodes exhibit excellent HER activities in 30 wt% KOH at 70 °C. The electrode produced with 100 µm Al foil achieved overpotentials of 117 mV and 142 mV at −0.5 A/cm$^2$ and −1 A/cm$^2$, respectively, outperforming uncoated Ni mesh by more than 290 mV. These values are comparable or superior to reported activities of Raney Ni-coated-electrodes in the literature.
- The enhanced activity is attributed to the significantly increased electrochemically active surface area, as demonstrated by normalized Tafel plots. No evidence of intrinsic catalytic improvements was found.
- Micro-flow cell testing of electrodes produced with 100 µm Al foil shows excellent performance with a stable cell voltage of 1.65 V at 0.5 A cm$^{-2}$ after 45 h, outperforming uncoated mesh by 324 mV.
- The presented material system exhibits a superior cell voltage compared to commercial Raney Ni electrodes.

Further investigation should focus on optimizing the Raney Ni layer thickness via the applied heat treatment protocol as the literature indicates an optimum layer thickness with regards to the electrodes activity and stability [21]. As discussed previously, this optimization needs to consider both the applied Al foil dosage and the heat treatment protocol, making a detailed analysis of the phase formation and growth during heat treatment desirable.

The demonstrated process provides a route for fabricating high-performance Raney Ni electrodes from standard materials. The process requires basic equipment, offers high potential for scale up, and produces electrodes with higher activity compared to commercial Raney Ni. Due to their mesh-based geometry, the electrodes are suitable for integration into zero-gap electrolyzers, making this approach a promising alternative to conventional routes that often require specialized equipment.

## CRediT authorship contribution statement

**Matthias Gramlich:** Writing – original draft, Visualization, Software, Methodology, Investigation, Formal analysis, Conceptualization. **Florian Jürries:** Writing – review & editing, Visualization, Investigation, Formal analysis. **Sebastian Hilbert:** Writing – review & editing, Validation. **Thomas Rauscher:** Validation, Resources. **Felix Heubner:** Writing – review & editing, Supervision, Resources, Funding acquisition. **Christian Bernäcker:** Writing – review & editing, Supervision, Project administration, Conceptualization. **Thomas Weißgärber:** Supervision.

## Declaration of competing interest

The authors declare that they have no known competing financial interests or personal relationships that could have appeared to influence the work reported in this paper.

## Acknowledgement

This work was supported by the project SkalPro (03EI3052A) founded by the German Federal Ministry for Economic Affairs and Energy.

The authors thank Clémence Muzelle, Elodie Boller and Fabien Léonard for technical support during the experiments at ESRF (BM05).

## Appendix A. Supplementary data

Supplementary data to this article can be found online at https://doi.org/10.1016/j.ijhydene.2026.153918.

## References

[1] Masson-Delmotte V, Zhai P, Pirani A. Climate change 2021. The physical science basis. Summary for policymakers. Geneva, Switzerland: IPCC; 2021 [Online]. Available: https://www.ipcc.ch/report/ar6/wg1/chapter/summary-for-policymakers/. [Accessed 2 August 2023].

[2] Wappler M, Unguder D, Lu X, Ohlmeyer H, Teschke H, Lueke W. Building the green hydrogen market – current state and outlook on green hydrogen demand and electrolyzer manufacturing. Int J Hydrogen Energy Sep. 2022;47(79):33551–70. https://doi.org/10.1016/j.ijhydene.2022.07.253.

[3] Chatenet M, et al. Water electrolysis - from textbook knowledge to the latest scientific strategies and industrial developments. Chem Soc Rev 2022;51(11): 4583–762. https://doi.org/10.1039/D0CS01079K.

[4] Smolinka T, Lehner F, Kiemel S. Studie IndWEDe Industrialisierung der Wasserelektrolyse in -Deutschland - -chancen und -Herausforderungen für nachhaltigen Wasserstoff für Verkehr, Strom und -Wärme. Berlin: NOW GmbH; 2018.

[5] European Comission. Critical raw materials resilience: charting a path towards greater security and sustainability. https://ec.europa.eu/docsroom/documents/42849. [Accessed 2 August 2023].

[6] Kibler LA. Hydrogen electrocatalysis. ChemPhysChem May 2006;7(5):985–91. https://doi.org/10.1002/cphc.200500646.

[7] Sapountzi FM, Gracia JM, Kees-J Weststrate CJ, Fredriksson HOA, Hans Niemantsverdriet JW. Electrocatalysts for the generation of hydrogen, oxygen and synthesis gas. Prog Energy Combust Sci Jan. 2017;58:1–35. https://doi.org/10.1016/j.pecs.2016.09.001.

[8] Bard AJ, Faulkner LR, White HS. Electrochemical methods - fundamentals and applications. UK: Wiley; 2022.

[9] Murray R. Method of producing finely-divided nickel. https://patents.google.com/patent/US1628190A/en. [Accessed 10 January 2024].

[10] Safizadeh F, Ghali E, Houlachi G. Electrocatalysis developments for hydrogen evolution reaction in alkaline solutions – a review. Int J Hydrogen Energy Jan. 2015;40(1):256–74. https://doi.org/10.1016/j.ijhydene.2014.10.109.

[11] Lohrberg K, Kohl P. Preparation and use of Raney-Ni activated cathodes for large scale hydrogen production. Electrochim Acta Nov. 1984;29(11):1557–61. https://doi.org/10.1016/0013-4686(84)85009-4.

[12] Tanaka S, Hirose N, Tanaki T, Ogata YH. Effect of Ni-Al precursor alloy on the catalytic activity for a Raney-Ni cathode. J Electrochem Soc 2000;147(6):2242. https://doi.org/10.1149/1.1393514.

[13] Chen L, Lasia A. Ni-Al powder electrocatalyst for hydrogen evolution - effect of heat-treatment on morphology, composition, and kinetics. J Electrochem Soc Sep. 1993;140(9):2464–73. https://doi.org/10.1149/1.2220845.

[14] Liu T, Reißner R, Schiller G, Ansar A. Experimental and numerical study of the effect of gas-shrouded plasma spraying on cathode coating of alkaline electrolysis cells. J Therm Spray Technol Jan. 2018;27(1–2):35–49. https://doi.org/10.1007/s11666-017-0654-2.

[15] Chade D, Berlouis L, Infield D, Nielsen PT, Mathiesen T. Deactivation mechanisms of atmospheric plasma spraying raney nickel electrodes. J Electrochem Soc 2016;163(3):F308–17. https://doi.org/10.1149/2.0091605jes.

[16] Marini S, et al. Advanced alkaline water electrolysis. Electrochim Acta Nov. 2012;82:384–91. https://doi.org/10.1016/j.electacta.2012.05.011.

[17] Balej J, Divisek J, Schmitz H, Mergel J. Preparation and properties of raney nickel electrodes on Ni-Zn base for H2 and O2 evolution from alkaline solutions part II: leaching (activation) of the Ni-Zn electrodeposits in concentrated KOH solutions and H2 and O2 overvoltage on activated Ni-Zn raney electrodes. J Appl Electrochem Aug. 1992;22(8):711–6. https://doi.org/10.1007/BF01027498.

[18] Bernäcker CI, Rauscher T, Büttner T, Kieback B, Röntzsch L. A powder metallurgy route to produce raney-nickel electrodes for alkaline water electrolysis. J Electrochem Soc 2019;166(6):F357–63. https://doi.org/10.1149/2.0851904jes.

[19] Kjartansdóttir CK, Nielsen LP, Møller P. Development of durable and efficient electrodes for large-scale alkaline water electrolysis. Int J Hydrogen Energy Jul. 2013;38(20):8221–31. https://doi.org/10.1016/j.ijhydene.2013.04.101.

[20] Schalenbach M, Kasian O, Mayrhofer KJJ. An alkaline water electrolyzer with nickel electrodes enables efficient high current density operation. Int J Hydrogen Energy Jul. 2018;43(27):11932–8. https://doi.org/10.1016/j.ijhydene.2018.04.219.

[21] Kjartansdóttir C, Caspersen M, Egelund S, Møller P. Electrochemical investigation of surface area effects on PVD Al-Ni as electrocatalyst for alkaline water electrolysis. Electrochim Acta Oct. 2014;142:324–35. https://doi.org/10.1016/j.electacta.2014.07.061.

[22] Schiller G, Henne R, Borck V. Vacuum plasma spraying of high-performance electrodes for alkaline water electrolysis. J Therm Spray Technol Jun. 1995;4(2):185–94. https://doi.org/10.1007/BF02646111.

[23] Günther T, Schick J, Körner T, Mangold T, Weihrich R. Simple process to nanostructured Raney-nickel electrodes for highly active and cost-efficient hydrogen evolution in alkaline water electrolysis (AWE). Int J Hydrogen Energy Mar. 2025:S0360319925009826. https://doi.org/10.1016/j.ijhydene.2025.02.398.

[24] Martínez WM, Fernández AM, Cano U, Sandoval J A. Synthesis of nickel-based skeletal catalyst for an alkaline electrolyzer. Int J Hydrogen Energy Aug. 2010;35(16):8457–62. https://doi.org/10.1016/j.ijhydene.2010.04.109.

[25] Los P, Rami A, Lasia A. Hydrogen evolution reaction on Ni-Al electrodes. J Appl Electrochem Feb. 1993;23(2):135–40. https://doi.org/10.1007/BF00246950.

[26] Chade D, Berlouis L, Infield D, Cruden A, Nielsen PT, Mathiesen T. Evaluation of raney nickel electrodes prepared by atmospheric plasma spraying for alkaline water electrolysers. Int J Hydrogen Energy Nov. 2013;38(34):14380–90. https://doi.org/10.1016/j.ijhydene.2013.09.012.

[27] Schiller G. High performance electrodes for an advanced intermittently operated 10-kW alkaline water electrolyzer. Int J Hydrogen Energy Sep. 1998;23(9):761–5. https://doi.org/10.1016/S0360-3199(97)00122-5.

[28] Chen L, Lasia A. Study of the kinetics of hydrogen evolution reaction on nickel-zinc alloy electrodes. J Electrochem Soc Nov. 1991;138(11):3321. https://doi.org/10.1149/1.2085409.

[29] Zhang J, et al. Electrochemical preparation and post-treatment of composite porous foam NiZn alloy electrodes with high activity for hydrogen evolution. Sci Rep Oct. 2018;8(1):15071. https://doi.org/10.1038/s41598-018-33205-4.

[30] Gannon WJF, Dunnill CW. Raney nickel 2.0: development of a high-performance bifunctional electrocatalyst. Electrochim Acta Nov. 2019;322:134687. https://doi.org/10.1016/j.electacta.2019.134687.

[31] Razmjooei F, et al. Improving plasma sprayed Raney-type nickel–molybdenum electrodes towards high-performance hydrogen evolution in alkaline medium. Sci Rep Jul. 2020;10(1):10948. https://doi.org/10.1038/s41598-020-67954-y.

[32] Kuang W, et al. Self-supported Ni/Ni(OH)$_2$ electrodes for high-performance alkaline and AEM water electrolysis. Adv Energy Mater Apr. 2025;15(14):2406080. https://doi.org/10.1002/aenm.202406080.

[33] Kraglund MR, et al. Ion-solvating membranes as a new approach towards high rate alkaline electrolyzers. Energy Environ Sci 2019;12(11):3313–8. https://doi.org/10.1039/C9EE00832B.

[34] Bernäcker CI, et al. Verfahren zur Herstellung einer Metallsubstrat-Katalysator-Einheit. https://register.dpma.de/DPMAregister/pat/register?AKZ=1020202047472&CURSOR=1; Nov. 27, 2025.

[35] Bakker ML, Young DJ, Wainwright MS. Selective leaching of NiAl3 and Ni2Al3 intermetallics to form raney nickels. J Mater Sci Nov. 1988;23(11):3921–6. https://doi.org/10.1007/BF01106814.

[36] Bernauer C, et al. Investigation of the cause-effect relationships between the exothermic reaction and the microstructures of reactive Ni-Al particles produced by high energy planetary ball milling. Metals Jun. 2021;11(6). https://doi.org/10.3390/met11060876.

[37] Konieczny M. Mechanical properties and deformation behavior of laminated Ni-(Ni2Al3+NiAl3) and Ni-(Ni3Al+NiAl) composites. Mater Sci Eng, A Dec. 2013;586:11–8. https://doi.org/10.1016/j.msea.2013.08.002.

[38] Smith AJ, Trimm DL. The preparation of skeletal catalysts. Annu Rev Mater Res Aug. 2005;35(1):127–42. https://doi.org/10.1146/annurev.matsci.35.102303.140758.

[39] Weitkamp T, Haas D, Wegrzynek D, Rack A. ANKAphase: software for single-distance phase retrieval from inline X-ray phase-contrast radiographs. J Synchrotron Radiat Jul. 2011;18(4):617–29. https://doi.org/10.1107/S0909049511002895.

[40] Tomwer — tomwer documentation. https://tomotools.gitlab-pages.esrf.fr/tomwer/index.html. [Accessed 10 April 2025].

[41] Paganin D, Mayo SC, Gureyev TE, Miller PR, Wilkins SW. Simultaneous phase and amplitude extraction from a single defocused image of a homogeneous object. J Microsc Apr. 2002;206(1):33–40. https://doi.org/10.1046/j.1365-2818.2002.01010.x.

[42] Schneider CA, Rasband WS, Eliceiri KW. NIH image to ImageJ: 25 years of image analysis. Nat Methods Jul. 2012;9(7):671–5. https://doi.org/10.1038/nmeth.2089.

[43] Trasatti S, Petrii OA. Real surface area measurements in electrochemistry. Pure Appl Chem Jan. 1991;63(5):711–34. https://doi.org/10.1351/pac199163050711.

[44] McCrory CCL, Jung S, Peters JC, Jaramillo TF. Benchmarking heterogeneous electrocatalysts for the oxygen evolution reaction. J Am Chem Soc Nov. 2013;135(45):16977–87. https://doi.org/10.1021/ja407115p.

[45] Li Z, et al. Seed-assisted formation of NiFe anode catalysts for anion exchange membrane water electrolysis at industrial-scale current density. Nat Catal Aug. 2024;7(8):944–52. https://doi.org/10.1038/s41929-024-01209-1.

[46] Prits A-V, et al. Electrochemical characterisation of raney nickel electrodes for alkaline water electrolysis: from laboratory to industrial scale. Int J Hydrogen Energy 2025;140:803–14. https://doi.org/10.1016/j.ijhydene.2025.05.262.

[47] Okamoto H. Al-Ni (aluminum-nickel). J Phase Equilibria Diffus Oct. 2004;25(4):394. https://doi.org/10.1007/s11669-004-0163-0.

[48] Du Y, Clavaguera N. Thermodynamic assessment of the al□ni system. J Alloys Compd Apr. 1996;237(1):20–32. https://doi.org/10.1016/0925-8388(95)02085-3.

[49] Ansara I, Dupin N, Lukas HL, Sundman B. Thermodynamic assessment of the Al-Ni system. J Alloys Compd Jan. 1997;247(1):20–30. https://doi.org/10.1016/S0925-8388(96)02652-7.

[50] Alimadadi H, Kjartansdóttir C, Burrows A, Kasama T, Møller P. Nickel-aluminum diffusion: a study of evolution of microstructure and phase. Mater Char Aug. 2017;130:105–12. https://doi.org/10.1016/j.matchar.2017.05.039.

[51] Philippe T, Erdeniz D, Dunand DC, Voorhees PW. A phase-field study of the aluminizing of nickel. Philos Mag Mar. 2015;95(9):935–47. https://doi.org/10.1080/14786435.2015.1010622.

[52] Ren X, Chen G, Zhou W, Wu C, Zhang J. Formation and growth kinetics of intermediate phases in Ni-Al diffusion couples. J Wuhan Univ Technol -Materials Sci Ed Oct. 2009;24(5):787–90. https://doi.org/10.1007/s11595-009-5787-9.

[53] Ertl G, Knozinger H, Weitkamp J. Preparation of solid catalysts. 1999.

[54] Boruciński Th, Rausch S, Wendt H. Raney nickel activated H2-cathodes part II: correlation of morphology and effective catalytic activity of Raney-nickel coated cathodes. J Appl Electrochem Nov. 1992;22(11):1031–8. https://doi.org/10.1007/BF01029581.

[55] Hall DS, Bock C, MacDougall BR. The electrochemistry of metallic nickel - oxides, hydroxides, hydrides and alkaline hydrogen evolution. J Electrochem Soc 2013;160(3):F235–43. https://doi.org/10.1149/2.026303jes.

[56] Demnitz M, Lamas YM, Garcia Barros RL, De Leeuw Den Bouter A, Van Der Schaaf J, Theodorus De Groot M. Effect of iron addition to the electrolyte on alkaline water electrolysis performance. iScience Jan. 2024;27(1):108695. https://doi.org/10.1016/j.isci.2023.108695.

[57] Mauer AE, Kirk DW, Thorpe SJ. The role of iron in the prevention of nickel electrode deactivation in alkaline electrolysis. Electrochim Acta Mar. 2007;52(11):3505–9. https://doi.org/10.1016/j.electacta.2006.10.037.

[58] Choi Y-I, Wang E-C, Kim H-A. Fabrication of highly porous raney Ni electrocatalyst using hot-dip galvanizing. Int J Hydrogen Energy Sep. 2025;165:150894. https://doi.org/10.1016/j.ijhydene.2025.150894.

[59] Lee HI, et al. Advanced Zirfon-type porous separator for a high-rate alkaline electrolyser operating in a dynamic mode. J Membr Sci Dec. 2020;616:118541. https://doi.org/10.1016/j.memsci.2020.118541.